An Empirical Predictive Model for Atmospheric H Lyman-α Emission Brightness at Mars

Majd Mayyasi[1*], Adil Mayyasi
majdm@bu.edu

* Corresponding Author
1 Center for Space Physics, Boston University, Boston, MA, USA

Journal: Earth and Space Science
Key Words: Mars, UV, Spectroscopy, Atmosphere, Escape, Water

Takeaways:

1) Nine years of H Ly-α brightness measurements are found to depend on solar cycle, illumination, and Martian season.
2) Statistical fits for H Ly-α brightness across independent variables are empirically derived.
3) A predictive tool for atmospheric H brightness at Mars is developed and shared with the community.

Abstract

Characterizing the abundance of atmospheric hydrogen (H) at Mars is critical for determining the current and, subsequently, the primordial water content on the planet. At present, the atmospheric abundance of Martian H is not directly measured but is simulated using proprietary models that are constrained with observations of H Lyman-α emission brightness, as well as with observations of other atmospheric parameters, such as temperature and solar UV irradiance. To make the data needed to model H abundances and escape rates more accessible to the community, this work utilizes over nine years of observations of H Lyman-α emissions made with the Mars Atmosphere and Volatile Evolution (MAVEN) mission. The H brightness in the upper atmosphere of Mars is analyzed for statistical variability across multiple variables and found to be dependent on solar illumination, solar cycle, and season. The resulting data trends are used to derive empirical fits to build a predictive framework for future observations or an extrapolative tool for primordial estimates. Data that was intentionally not included in the empirical derivations are used to validate the predictions and found to reproduce the H Lyman-α brightness to within 18% accuracy, on average. This first of its kind predictive model for H brightness is presented to the community and can be used with atmospheric models to further derive and interpret the abundances and escape rate of H atoms at Mars.

Plain Language Summary

The upper atmosphere of Mars contains Hydrogen atoms that can escape into outer space. Since these atoms originate from water, understanding the abundance and variation in these atoms is important to understanding water escape from Mars. This work investigates the properties of H atoms at Mars to predict their variations with time and to better understand

44 how they may have changed over the history of the planet.

Introduction

Estimating the primordial water content at Mars is an involved undertaking that requires a comprehensive understanding of water variability in the present epoch using multiple synergistic observations and interpretations [e.g., Jakosky, 2021]. The reservoir of escaping atmospheric species lies in the upper atmosphere of Mars. As water molecules propagate from surface to space, solar photons and chemical reactions dissociate the molecules into their atomic constituents, providing additional markers to observe, such as atomic hydrogen, deuterium, and oxygen [e.g., Clarke et al., 2014; Fedorova et al., 2021; Heavens et al., 2018; Krasnopolsky, 2019; Stone et al., 2020]. The water cycle, and subsequently the abundance of H atoms in the atmosphere, is affected by multiple drivers, such as: surface dynamics, circulation patterns, cloud interactions, seasonal variations, dust activity, atmospheric tides and waves, atmospheric chemistry, illumination conditions, and solar activity [e.g., Heavens et al., 2018; Montmessin et al., 2022]. These drivers can cause atmospheric properties to vary at timescales that range from days to many years. To determine water loss at Mars requires quantifying how the upper atmospheric H atoms are expected vary across these various timescales.

Ultraviolet (UV) spectroscopy is used to observe H Lyman-α emissions from water-originating hydrogen atoms in the upper atmosphere of Mars. Hydrogen atoms produce UV emissions at 1215.67 Å when solar photons resonantly scatter off the atoms. These H emissions can be observed and used to derive a line-of-sight brightness value when compared with a calibrated source [e.g., Mayyasi et al., 2017; 2023]. The H Lyman-α emission at Mars is optically thick and can be interpreted by using radiative transfer techniques [e.g., Anderson and Hord, 1977; Gladstone, 1982]. These radiative transfer techniques typically include multiple simplifying assumptions to derive an estimated column of atoms along the line-of-sight from the observed brightness [Chaufray et al., 2008; 2021; Chaffin et al., 2018; Bhattacharyya et al., 2020].

H atoms' emission brightness, abundances, and escape rates are not physically interchangeable quantities. Extreme solar weather events and planetary dust storms are extrinsic and intrinsic examples, respectively, of what may induce higher H escape rates at the planet [e.g., Mayyasi et. al, 2018; Chaffin et al., 2017; 2021]. However, the brightness and abundance of the upper atmospheric H Lyman-α emissions may not vary as similarly [e.g., Mayyasi et al., 2023]. UV spectroscopy measures the H emission brightness. Radiative transfer simulation results are then used to determine the column of atoms along the line-of-sight that would reproduce the observed emissions and use that as an estimate for the atmospheric abundance of H atoms.

The motivation for this work is to determine what observable trends in Martian H Lyman-α emissions can be independently derived and predicted for further interpretation within the scientific community. We therefore characterize the variability in H Lyman-α brightness measurements by analyzing over nine years of data obtained from the upper atmosphere of Mars. The variation in the data with time, topology, and observational conditions are used to develop statistical trends with empirical fits. The empirical fits are interpolated to make a predictive model of H brightness in the upper atmosphere of Mars. Predictions are made and then compared with new data to assess reproducibility.

The empirical and predictive framework developed and presented in this work is made available to the planetary and exoplanetary radiative transfer modeling community to support independent derivations of the atomic H content in the upper atmosphere of Mars and other Mars-like bodies. This tool can be used to derive the abundance and escape rate of H atoms as well as to constrain water content in the Martian upper atmosphere to support further interpretation of its variability.

Data and Methods

The MAVEN mission carries a remote sensing Imaging Ultraviolet Spectrograph (IUVS) instrument [Jakosky et al., 2015]. The IUVS instrument measures H Lyman-α brightness in low spectral resolution (FUV) mode, and measures H and D Lyman-α brightness in high spectral resolution echelle (ECH) mode [McClintock et al., 2014]. In this study, the ECH mode data are used to support future studies that analyze ECH-measured deuterium as well as spectrally resolved oxygen doublet and triplet emissions that would be more directly comparable to this dataset. IUVS ECH data cover disk and limb observations of the planet. Since the H Lyman-α observations made of the Martian limb can include non-negligible contributions from Interplanetary Hydrogen (IPH) emissions, this study only utilizes disk-pointed observations where the IPH emissions are negligible along the line-of-sight [Mayyasi et al., 2023].

The Martian H corona spans several planetary radii that extend beyond the orbital altitude of the MAVEN spacecraft [Nagy et al., 1990; Chaufray et al., 2008]. Subsequently, the IUVS ECH disk-pointed observations include a significant amount of illuminated H atoms that are resonantly scattering solar photons, even when the line-of-sight is pointed at the night-side of the planet. This observational geometry results in a comprehensive dataset of H Lyman-α emission brightness across illumination conditions. The dataset spans the last third of Mars Year (MY) 32 through the first third of MY37. During the MAVEN observational timeline, the solar cycle ranged from maximum to minimum of Solar Cycle 24 and continued through the increasing activity phase of Solar Cycle 25. The dataset used here therefore also represents a range of solar activities.

The IUVS echelle mode observations are optimized for orders of H and D Lyman-α that reflect off an echelle grating onto a 1024x1024 pixel detector [McClintock et al., 2014]. The observed photon counts are reduced and integrated across the aperture and spectral range to obtain a brightness, in kilo-Rayleigh (kR) [e.g., Mayyasi et al., 2017]. Earlier in the mission lifetime, the detector-binning schemes, voltage gain setting, and exposure time were varied to maximize data yield for the optical configuration. Here we use data from when these settings settled to their optimal values: a 332$\times$74 spectral$\times$spatial binning scheme, a voltage gain of 796.29 Volts, and an exposure time of 29.0 seconds. Two disk-pointed echelle observations are typically obtained for each orbit: one on the inbound segment of the orbit (leading up to spacecraft periapsis) and one on the outbound leg of the orbit (following spacecraft periapsis). The data

from each orbit include between 8 and 20 exposures. For H observations, the data from each exposure in a single orbital segment are averaged to obtain one data point.

MAVEN has been in orbit around Mars since September 2014. This work utilizes observations made between November 2014 and May 2023. The dataset used to obtain empirical trends spans Nov 12th, 2014 (orbit 240), through Feb 14th, 2023 (orbit 18202), and include 6529 data points. The dataset used exclusively to compare with predictions span Feb 15th, 2023 (orbit 18210), through May 14th, 2023 (orbit 18794) and include 185 data points.

A statistical approach was used to derive H brightness trends. The H brightness is the dependent variable (labeled as Y). The H brightness values, derived across the mission timeline, were examined for dependance on several observable variables, listed in Table 1 as X1, X2, X3, etc. Variables that showed no obvious trends in Y were ruled out. Variables that did show obvious trends with Y were then further investigated for inter-dependance. A functional form was used to fit the empirical trends to the resulting sub-set of variables using a functional form with first-order estimates that was then optimized using minimum square variance to produce a best-fit. The resulting best-fit functional form was then used to predict values of H brightness. A subset of data (last 3 months) was intentionally excluded from the empirical analysis so that it could be used exclusively to test the predictive capabilities of the model.

Table 1. Variables used to examine (inter)dependency on H Lyman-α brightness.

Variable	Observable	Definition
X1	SZA	Solar Zenith Angle
X2	Ls	Solar Longitude
X3	LT	Local Time
X4	SI	Solar Irradiance
X5	EA	Emission Angle
X6	Lat	Latitude
X7	Lon	Longitude
X8	SC	Spacecraft Altitude

The variables in **Table 1** were chosen based on their potential to directly impact the variability of H brightness along the observational line of sight. Solar zenith angle and local time are expected to impact the illumination along the column of H atoms as these represent how much overhead illumination the atmosphere is subjected to. Solar longitude and solar irradiance (also used to account for Solar Cycle) are expected to affect the incident upper atmospheric photon flux that can interact with H atoms and so are also considered as candidate variables to analyze.

Observations were filtered for a low emission angle (deviation of the line-of-sight from nadir) of <40° to minimize longer path lengths across a non-uniform atmosphere, and so, the deviation from strictly nadir observing (EA of 0°) up to 40° was examined as a potential impactor of H brightness. Latitude and Longitude were also evaluated for potential topographical effects on upper atmospheric H brightness. The altitude of the MAVEN spacecraft in its orbit during the

observations was also examined to account for any biases in the observing conditions. Other variables such as: integration time of the observations and observational segment (e.g., inbound vs outbound), were investigated for completeness but had no effects on H brightness trends.

Results and Discussion

The H emission brightness from the co-added MAVEN IUVS ECH mode disk observations are shown in **Figure 1**. The brightness varies between 0.18 kR and 12.79 kR throughout the mission timeline and can change with multiple timescales. The observations were made during both inbound and outbound segments of the orbit, where illumination conditions are different, resulting in two data points from the same orbit having different brightness values. Furthermore, a Mars year spans 687 days, where the planetary distance from the Sun varies, resulting in variations in the solar irradiation-sensitive H brightness values. Added to these drivers, the solar cycle transitioned from maximum to minimum to another maximum across the timeline, providing an additional timescale for the variability in the observed atmospheric H brightness.

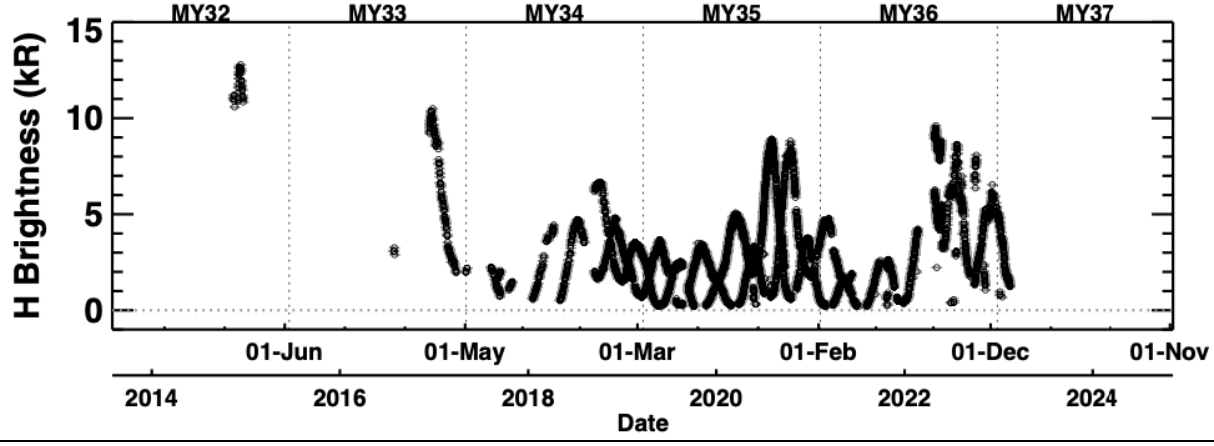

Figure 1. H Lyman-α emission brightness in kR (black circles), averaged over each orbital segment, plotted as a function of mission timeline. Measurement uncertainties are shown as grey error bars and are negligible for the H Lyman-α emissions in this dataset.

Mars encounters regional and global dust storms during its perihelion season (Ls ~180°–360°) that could affect the observed upper atmospheric H brightness from year to year. Studies have shown that a global dust storm can heat up and inflate the dominant and heavier species in the atmosphere (namely, CO_2). This atmospheric expansion leads to higher collision frequencies within atmospheric constituents and subsequently more suppression of H atoms that would otherwise have diffused more freely to higher altitudes [e.g., Mayyasi et al., 2018]. Other studies have further shown minimal effects of dust-storms on H atomic abundances in the upper atmosphere [Holmes et al., 2021]. While the abundance of H atoms may or may not be

affected by dust storms, the H Lyman-α brightness does vary with a trend that is different from one MY to the next [Mayyasi et al., 2023].

H Brightness Dependencies

To understand, quantify, and predict the H brightness as a function of time (through the MAVEN mission timeline and beyond), the H brightness was examined against the observational variables listed in **Table 1** to isolate the most dominant drivers of variability and to derive a functional form for the trends in the data. The first four variables, X1 through X4, resulted in the clearest trends, as shown in **Figure 2**.

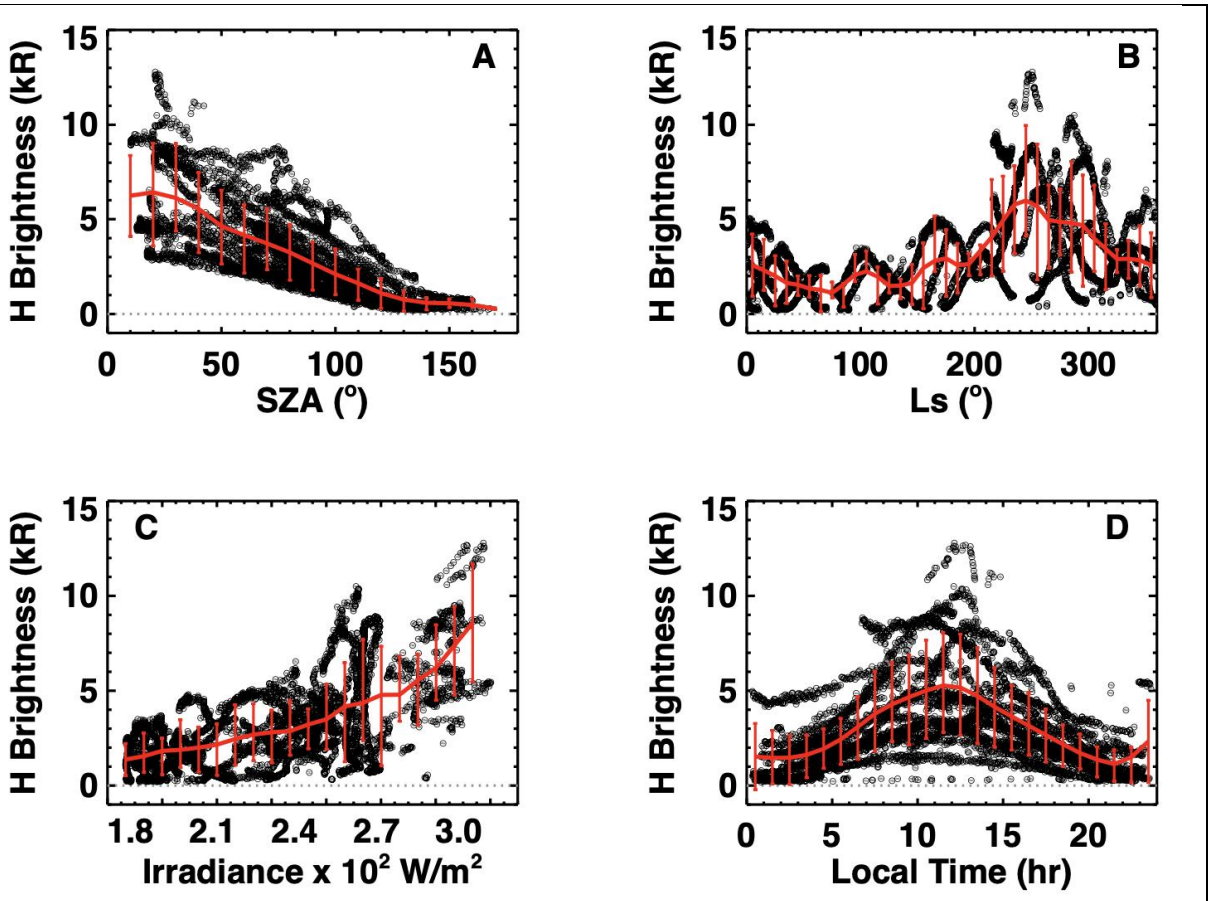

Figure 2. Nine+ years of H Lyman-α emission brightness collected by MAVEN and examined for dependencies on observational variables. (A) H brightness as a function of Solar Zenith Angle (black circles) is shown with averages and standard deviations (red vertical lines) for 18×10° bins with a fit to the average (red trendline). (B) H brightness as a function of Solar Longitude (black circles) is shown with averages and standard deviations (red vertical lines) for 36×10° bins with a fit to the average (red trendline). (C) H brightness as a function of Solar Irradiance (black circles) is shown with averages and standard deviations (red vertical lines) for 20× 6.7E-4 W/m^2 bins with a fit to the average (red trendline). (D) H brightness as a function of Local Time (black circles) is shown with averages and standard deviations (red

vertical lines) for 24×1 hr bins with a fit to the average (red trendline).

SZA measures the angle between the observational tangent point on the surface along the instrument line of sight, and a vector from the tangent point to the Sun. In this dataset, the SZA ranges between 10.18° and 167.8°. H Lyman-α emissions are therefore brightest when the Sun is nearest to being overhead at low SZA and become faintest on the nightside at higher SZA when much of the line of sight within the atmosphere is in the shadow of the planet. This trend of decreasing brightness with increasing SZA is evident in the data (**Fig 2A**). At high SZA, the brightness converges to low values, and at low SZA, the brightness increases and forms divergent trends. In binning the H brightness by 10° in SZA, averages with standard deviations from the mean showed the variance to range from a maximum of $\pm$ 2.5 kR at SZA < 40° to a minimum of $\pm$ 0.3 kR at SZA > 140°. This divergence in brightness is likely due to variations in other parameters such as season and solar cycle in each 10° SZA bin, as is described next.

The Solar longitude in the observations varies between 0.0634° and 359.96°. Aphelion season at Mars is when the planet is farther from the Sun in its orbit, between 0° and 180° Ls. Perihelion season at Mars is when the planet is closer to the Sun in its orbit, between 180° and 360° Ls. The trend in the data of **Fig 2B** shows a significant amount of smaller scale variability that is attributed to SZA, and shows fainter H emissions at aphelion than at perihelion season, due to the proximity of the planet to the Sun. Binning the H brightness by 10° bins in Ls and taking the average and standard deviation in brightness for each bin showed a variance that ranged from a minimum of $\pm$ 0.8 kR at Ls < 180° and a maximum of $\pm$ 5.5 kR at Ls > 180°. The large spread in the data is attributed to the varying SZA as well as the timing of perihelion season's onset of dust storms that can begin between 165° and 210° Ls and can end between 280° and 310° Ls [Kass et al., 2016; 2019].

Solar irradiance at Mars is measured in situ using the MAVEN Extreme Ultraviolet Monitor (EUVM) instrument [Eparvier et al., 2015]. For these observations, the values obtained from the Lyman-α channel of the EUVM instrument range between 1.866×10^{2} W/m^{-2} and 3.202×10^{-2} W/m^{2}. The plot in **Fig 2C** shows a trend of increasing H Lyman-α brightness as solar irradiance increases, as expected. H brightness values were binned by 6.7×10^{-4} W/m^{2} to obtain the average and variance in SI within each bin and was found to range between $\pm$ 0.75 kR and $\pm$ 3.5 kR. This trend compounds the effects of a changing solar cycle throughout the timeline of MAVEN observations with the effects of changing orbital location. The next section addresses the interdependencies of these two effects.

The local time in the observations combines the effects of SZA, location on the surface, and declination of Mars as measured at the line of sight tangent point. In these observations, the local time ranged between 0.33 h and 23.65 h. The trends shown in **Fig 2D** show an increasing H brightness at local noon that tapers off to lower values during local nighttime. Binning the H brightness values into 1-hour bins in LT and taking the average and variance in each bin showed a spread ranging from a minimum of $\pm$ 1 kR at nighttime to a maximum of $\pm$ 2.5 kR during local

noon. The effects of local time are compounded with SZA and will be addressed in the next section on interdependencies.

H brightness variations against the remaining variables in **Table 1** (X5 – X9) are shown in the supplemental material (**Figure S1**) for completeness. The data showed significant scatter with these variables. While the range of values for H brightness do not change based on what variable they are examined against, the spread in the data indicated no obvious trendlines when compared with changing emission angle, latitude, longitude, and spacecraft altitude.

Interdependencies

To derive a functional form that can be used to represent (and predict) H brightness, the leading variables (SZA, LT, Ls, and SI) are first investigated to account for potential interdependencies. SZA and LT are interdependent as the former is derived from a combination of the latter, declination of the Sun, and latitude. For this dataset, the SZA is smallest at local noon conditions and increases closest to local midnight, as shown in **Figure 3A**. To account for this, we opt for using the SZA over LT as the preferred independent variable.

Due to Mars' elliptical orbit, there is a dependence expected for Solar Irradiance with Solar Longitude. As shown in **Figure 3B**, the Solar Irradiance observed at Mars depicts a few trends with solar longitude. The small scale sinusoidal variability in SI that spans ~20° in Ls throughout the Mars Year is due to the solar rotation period. The larger scale sinusoidal variability in SI is due to Mars' location in its elliptical orbit. The variability in SI from one MY to the next is due to varying solar activity in Solar Cycles 24 and 25.

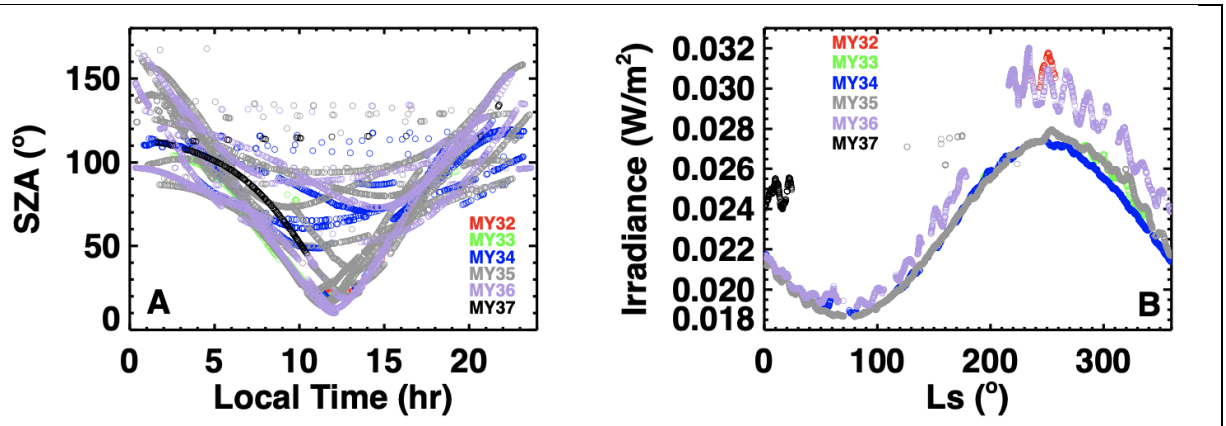

Figure 3. Interdependencies in the H brightness drivers show a (A) SZA dependence on LT, and a (B) Solar Irradiance dependence on Ls. The colors represent data collected in different Mars Years with MY32 data shown in red, MY33 data shown in green, MY34 data shown in blue, MY35 data shown in grey, MY36 data shown in purple, and MY37 data shown in black.

While no other interdependencies are expected in the remaining variables (SZA vs Ls, SZA vs SI, SI vs LT, and Ls vs LT), these are examined for due diligence (and shown in Supplemental

Material **Figure S2**). As expected, these variables displayed no appreciable trends, validating their independence.

Functional Representation

The distilled variables considered to drive H Lyman-α emission brightness are SZA, Ls, and Solar Cycle. To parametrize the data, two phases of the solar cycle are broadly considered: Solar Minimum and Solar Maximum. Observations considered for Solar Min are those made between June 18 2018, and April 2 2022. Observations considered for Solar Max are those bookending Solar Min, made between the earliest MAVEN ECH data acquired on November 12 2014, through June 17 2018, and between April 3 2022, through February 15 2023. Of the total 6529 data points used in this analysis, 5508 are obtained during Solar Min, and 1021 are obtained at Solar Max.

Solar longitude spans between 0° and 360° and is binned into 10° bins. In this binning scheme, all 36×10° Ls bins have solar minimum data, with the number of datapoints ranging between 21 and 221. Not all Ls bins have solar maximum data. The number of datapoints in populated bins range between 15 and 198. As MAVEN continues to make observations, these solar activity gaps will be filled in. The resulting data points for H brightness vs SZA for each bin and at each solar activity are then fit to a curve. An S-curve was found to be representative of the empirical trends, and can be formulated as:

$$Y(x) = A\left[1 - \frac{1}{1+e^{-Bx}}\right]^{C} \qquad \text{Equation (1)}$$

Where Y is the H brightness in kR, x is the SZA in degrees, and A, B and C are constants that are given ad hoc initial estimates A_i, B_i, and C_i. The initial estimates are varied incrementally by stepping less than and greater than their initial values over a total set of A_n, B_n, and C_n values. An iteration algorithm steps through all the combination of values for A_n, B_n, and C_n to generate a curve and calculate its variance to the data, χ^2. The combination of A_n, B_n, and C_n constants that produces the minimum variance are used as the optimal and final set of constants (A_f, B_f, and C_f) that are then used to generate the best-fit curve to the data in each bin.

B_i was the least sensitive constant to the curve fits and was taken to be 0.03 for all the bins. The initial values of A and C constants, used as first estimates for each bin, are shown in **Table 2**. The A and C constants were varied by 0.5 between ±4.0 of their initial estimates. The B constant was varied by 0.005 between ±0.025 of its initial value.

Table 2. First estimates of fitting constants used in the iterative fits to the data.

Solar Activity	Ls Bin	A_i	C_i
Min	<180°	4.5	6.0
	210°-230°	5.0	7.0

	270°-280°	10	7.0
	300°-310°	10	9.0
	All other bins	7.0	6.0
Max	<180°	6.0	9.5
	280°-290°, 300°-310°	14	10
	All other bins	8.0	14

The resulting best-fit curves and the data for all the bins are shown in **Figure 4**, offset along the y-axis for visibility. The best fit curves generally did well to reproduce the H brightness trends with SZA. The individual binned data and their fits are shown in the Supplemental Material (**Figure S3**).

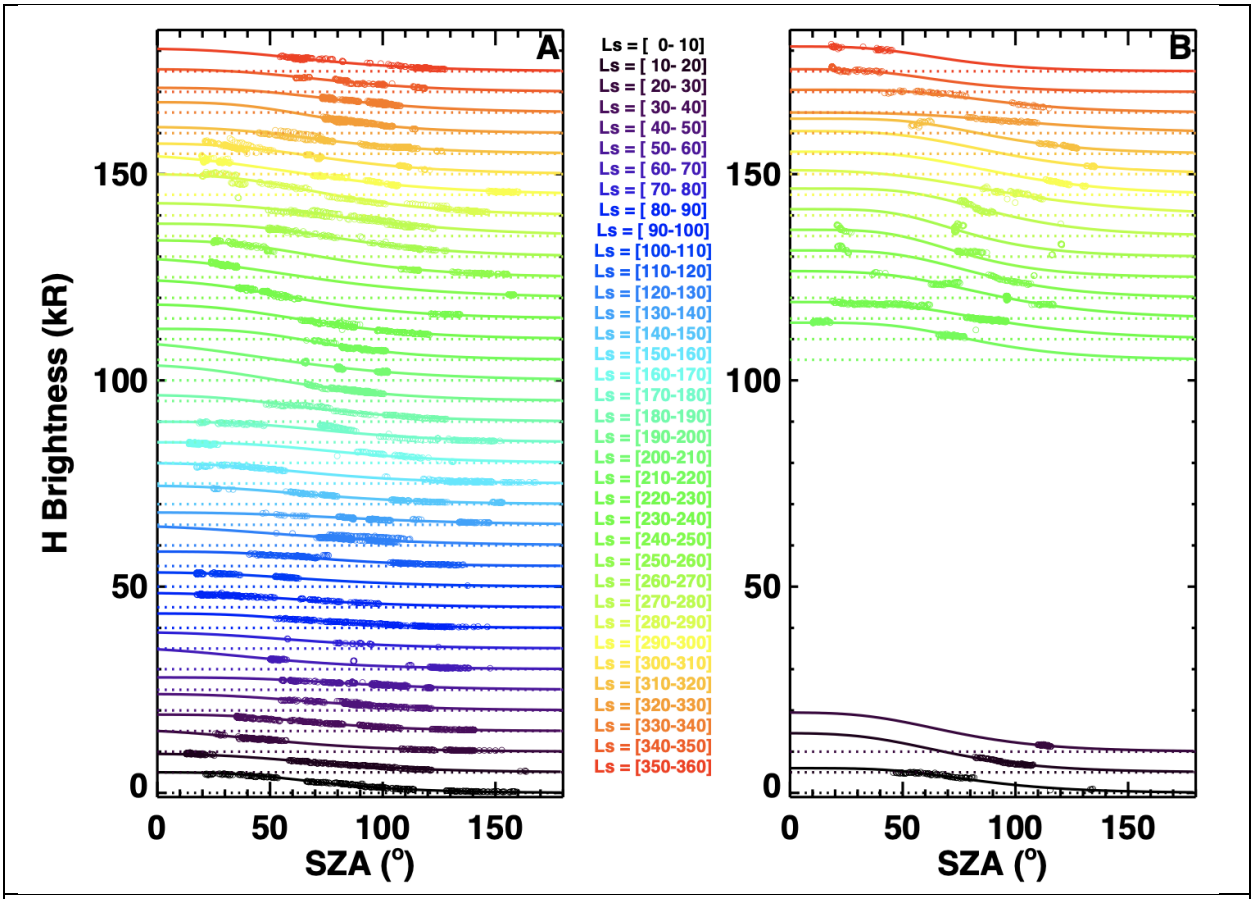

Figure 4. H brightness with SZA all bins in Ls, color coded by the legend in the center. Circles indicate H brightness measurements obtained for that Ls bin at (A) Solar Min and (B) Solar Max. Lines with the same color code as the data show the best fit curves for the data in that bin. A horizontal dotted line in all the panels indicates the zero brightness level. The data, fits, and zero-level for each bin are offset by 5 kR along the vertical axis for visibility.

Data Parametrization and Interpolations

The best-fit constants (A_f, B_f, and C_f) used to derive the optimal fitting curves are shown in **Figure 5**. During Solar Min, the best fit A_f constant varied throughout the Mars Year with a clear annual trend. The B_f constant was generally the same as the initial estimate, with few deviations above its average of 0.03. The C_f constant had significant scatter above its average value of 6.74. During Solar Max, the best fit A_f constant varied with Ls with a similar trend to its solar minimum counterpart, where data existed. The B_f constant averaged to 0.034. The C_f constant had significant scatter above its average value of 12.6.

An empirically derived trend is fit to the A values resulting from the binned fits for solar minimum, where data is available for all bins. Since the MAVEN data at solar maximum aphelion is still pending at the time of this writing, this empirical fit from solar minimum is scaled to fit the solar maximum A values, as constrained by existing data. These empirical fits for the A value, as well as the average B and C values from each solar activity case are used to extrapolate the curves into regions where no data exist, to make predictions for the upper atmospheric H emission brightness at Mars.

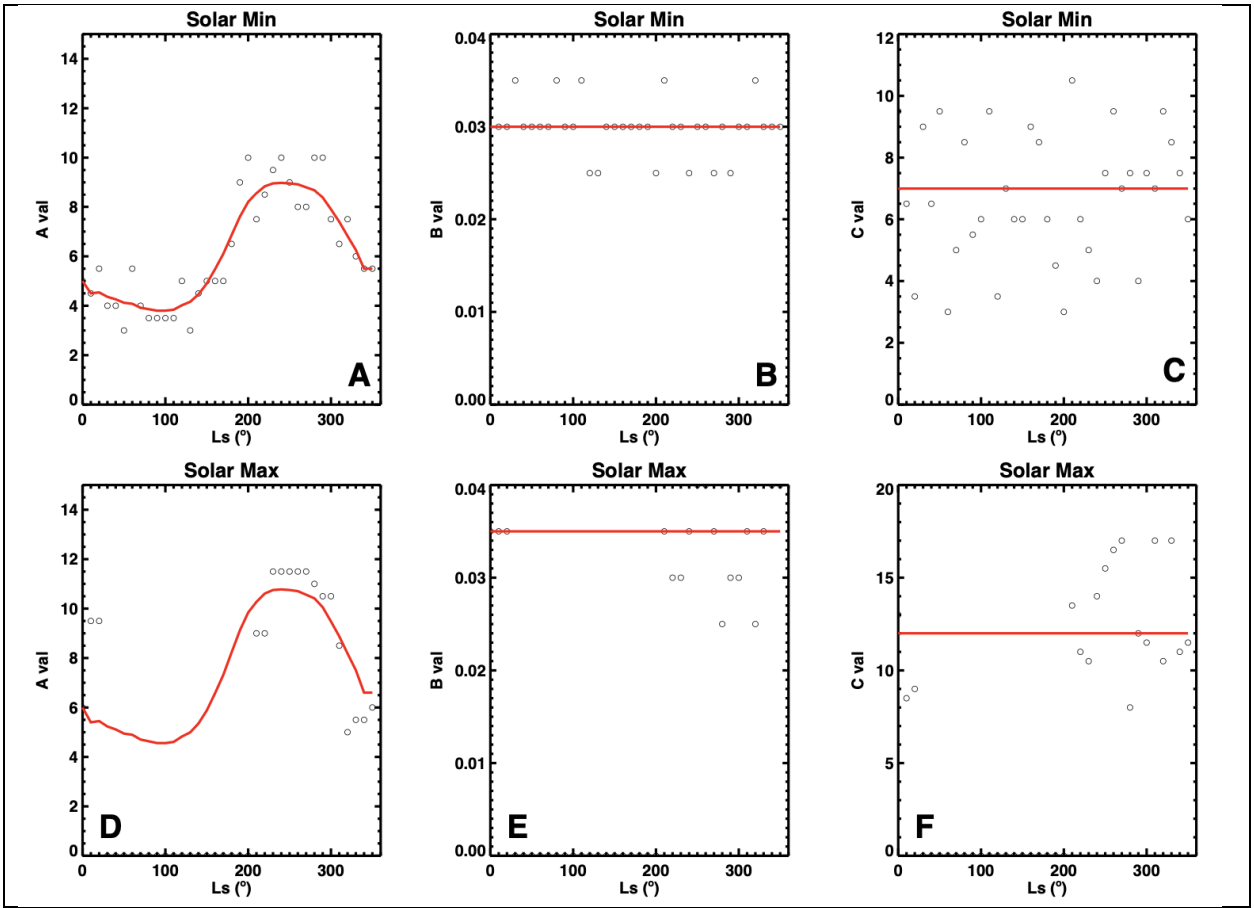

Figure 5. Final values (black circles) of the variables used to generate the optimal fits to the data. The top row shows Solar minimum constants A, B and C in unintentionally similarly named panels (A), (B) and (C), respectively. The bottom row shows Solar maximum constants A, B and C in panels (D), (E) and (F), respectively. The A constant (Left Column), B constant (Middle Column) and C constant (Right Column) show the values used in Eq (1) for each Ls

bin. The red lines in each panel are fits to the trends in A, B and C constants.

Adopting the empirical and scaled fits to the A constant and using the averages for the B and C constant (i.e., the red curves in **Fig. 5**) provided the range of values to use for predictive modeling of what the H emission brightness would be. A comparison of empirical fits and predicted fits to the H brightness for Solar Min and Solar Max conditions, and all 36×10° Ls bin is shown in the Supplemental Material (**Figures S4-S6**).

Validation and Predictions

The observational conditions (SZA, Ls, and Solar Cycle) were used to reproduce the data using the best-fit parameters derived from the empirical fits, the interpolated fits, and the predictions from the interpolated fits (**Figure 6**). Data that was not used in the parent dataset from which the empirical fits were derived were used as 'new data' to compare with predictive data.

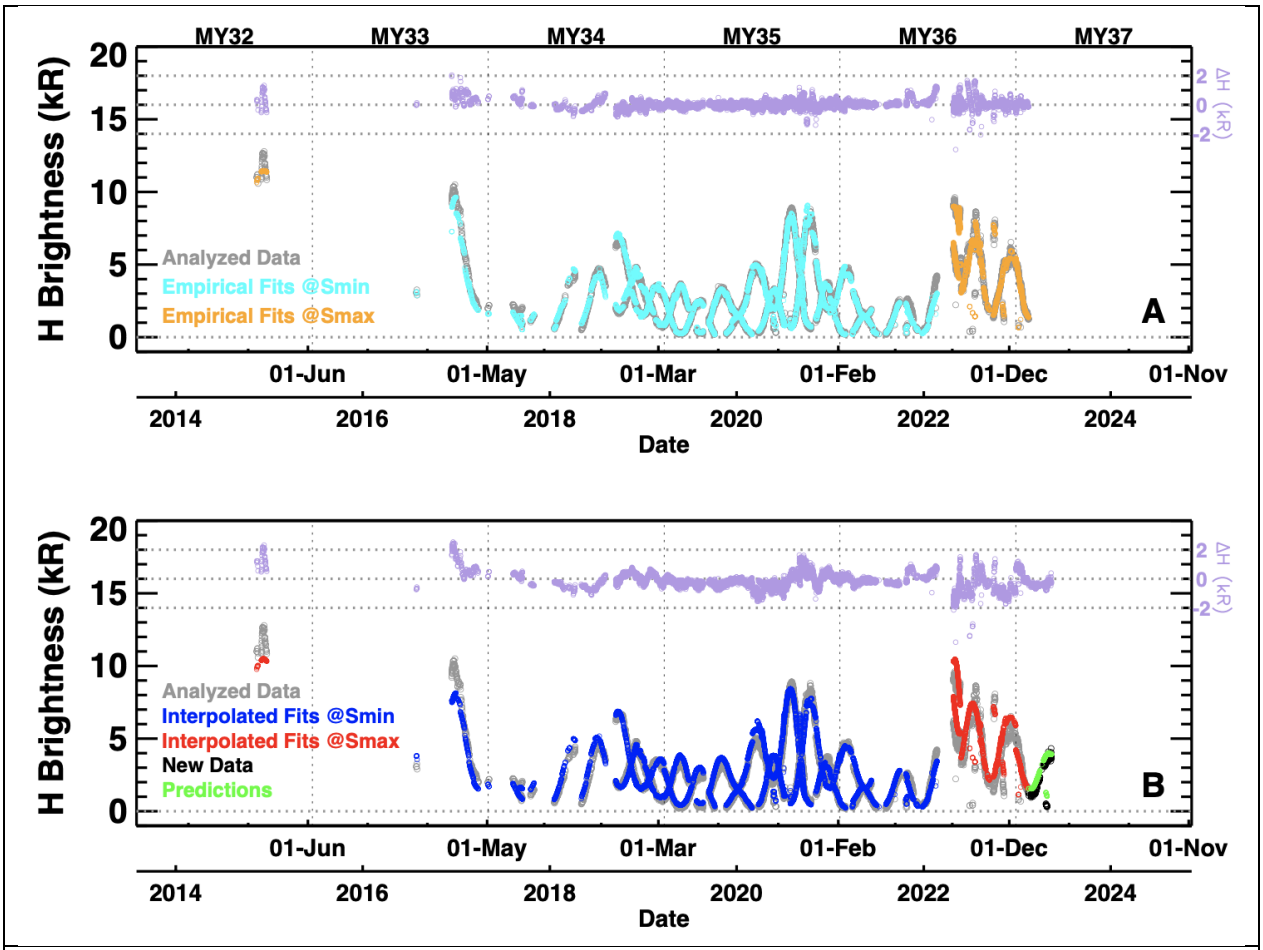

Figure 6. Disk-pointed MAVEN ECH observations of H Lyman-α emission brightness across the mission timeline spanning MY32-MY37, averaged for each orbital segment (grey circles). (A) H brightness values derived using the empirical best-fits to the data for Solar Minimum (light blue circles) and Solar Maximum (yellow circles). (B) H brightness values derived using the

interpolated best-fits for Solar Minimum (blue circles) and for Solar Maximum (red circles). New data (black circles) not used in the previous analysis collected by MAVEN ECH during Solar Max conditions with the values predicted from the interpolated fits (green circles). In both panels, the difference between the observed and fit data (ΔH) are shown in violet circles, vertically offset by 16 kR for visibility. A horizontal dotted lines at 0 kR denotes the zero-level for H brightness in the data. Horizontal lines at 14 kR, 16 kR, and 18 kR denote the -2, 0 and +2 kR levels for the difference (ΔH) as indicated on the offset right y-axis.

The empirical fits (**Fig 6A**) reproduced the data well, as expected from the best-fit derivations for both solar maximum and solar minimum conditions. Deviations from the data were within ~2 kR, and were largest during perihelion conditions, when variable dust storms impacted the atmosphere and likely affected the circulation patterns the propagate water molecules to the upper atmosphere where they break down to from atomic H. Similarly, the predictive model (**Fig 6B**) was able to reproduce the data to within ~2 kR, with the largest discrepancies occurring around perihelion season of each Mars Year.

Relatively newer-acquired data that was not included in the empirical fit derivations was used to further validate the predictions. This data was obtained at Solar maximum aphelion and was reproduced by the predictive model to within <0.5 kR (**Fig 6B**). These comparisons demonstrate the utility of the predictive model in simulating the H Lyman-α emission brightness in the upper atmosphere of Mars for the present-day epoch.

Note that dust storm effects on H brightness are not analyzed in this work. Regional dust storms at Mars vary from year to year and the predictability of the start, peak, and end date of these events is currently unreliable [e.g., Pieris and Hayne, 2023]. The variations in the trends and the parametrized projections found in this work would provide helpful predictions during solar minimum and/or aphelion conditions with more certainty than during solar maximum/perihelion conditions, due to the present dearth of empirical constraints in the latter scenario. With the availability of more MAVEN ECH data, the statistical trends would become more robust.

Conclusion

The empirically derived best-fit curves to the data reproduced the trends in H brightness to within 6%, on average, for Solar Minimum, and to within 9%, on average, for Solar Maximum. The discrepancies between the data and the empirical fits are negligible at aphelion (< 0.5 kR) and relatively small at perihelion (<~2 kR) when the H brightness tends to be highest. These discrepancies are due to the unpredictable variability in dust activity onset from one MY to another during perihelion that resulted in a scatter in the data in dusty Ls seasons. The interpolated best-fit curves to the data reproduced the data to within 6%, on average, for Solar Minimum, and to within 13%, on average, for Solar Maximum. The interpolated best-fit curves were able to predict new data at aphelion to within <0.5 kR (18%) on average. This accuracy is expected to improve at Solar Minimum conditions.

As additional MAVEN ECH data become available, the empirical derivations can continue to be supplemented (especially at Solar Maximum perihelion, where there is a current absence of data) to provide a more comprehensive empirical baseline for predictions.

The methodology developed here can further be applied to other planetary systems with extended H atmospheres and/or Mars-like exoplanets orbiting Sun-like stars. Specifically, the predictive tool developed here is the first critical step towards developing a consistent set of psychometric charts to evaluate the volatility of the Martian atmosphere as it relates to Hydrogen. H Lyman-α emission brightness is a fundamental quantity used with radiative transfer modeling tools to derive water escape. Specifically, the predictions developed here can be combined with others that measure ambient temperature and solar irradiance along the observational line of sight to calculate the abundance of H atoms in the atmosphere of Mars and to further derive the escape rates of H atoms from the planet. These results provide an empirical baseline for present-day conditions at Mars that could be used to extrapolate to primordial conditions.

Open Research

The MAVEN ECH data used in this study are available as fits files on the NASA PDS Atmospheres Node at: https:// pds-atmospheres.nmsu.edu/data_and_services/atmospheres_data/MAVEN/maven_main.html. IUVS echelle level1a v13 data were used. The methodology to reduce the data are described in detail in previous publications [Mayyasi et al., 2017; 2022] under doi: 10.1002/2016JA023466, and 10.1029/2022EA002602, respectively. The methodology required to reproduce the results in this work are self-contained in this manuscript.

Acknowledgement

This work was funded, in part, by NASA contract #1000320450 from the University of Colorado to Boston University.

References

Jakosky et al., (2015) Science, 350, 6261, 643–644.
McClintock et al., (2014) Space Sc. Rev., doi:10.1007/s11214-014-0098-7.

Anderson, D. E., & Hord, C. W. (1977). Multidimensional radiative transfer: Applications to planetary coronae. Planetary and Space Science, 25(6), 563–571. https://doi.org/10.1016/0032-0633(77)90063-0.

Bhattacharyya, D., J.Y. Chaufray, M. Mayyasi, J.T. Clarke, S. Stone, R.V. Yelle, W. Pryor, J.L. Bertaux, J. Deighan, S.K. Jain, N.M. Schneider (2020), Two-dimensional model for the martian exosphere: Applications to hydrogen and deuterium Lyman α observations, Icarus, 339, 113573, doi.org/10.1016/j.icarus.2019.113573.

Clarke, J. T., Bertaux, J.-L., Chaufray, J.-Y., Gladstone, G. R., Quemerais, E., Wilson, J. K., & Bhattacharyya, D. (2014). A rapid decrease of the hydrogen corona of Mars: The Martian hydrogen corona. Geophysical Research Letters, 41(22), 8013–8020. doi.org/10.1002/2014GL061803

Chaffin, M. S., Chaufray, J. Y., Deighan, J., Schneider, N. M., Mayyasi, M., Clarke, J. T., et al. (2018). Mars H escape rates derived from MAVEN/IUVS lyman alpha brightness measurements and their dependence on model assumptions. Journal of Geophysical Research: Planets, 123, 2192–2210. https://doi.org/10.1029/2018je005574

Chaffin, M.S. et al. (2021), Martian water loss to space enhanced by regional dust storms, Nat. Astro., v 5, 1036–1042, doi.org/10.1038/s41550-021-01425-w

Chaufray, J. Y., Bertaux, J. L., Leblanc, F., & Quémerais, E. (2008). Observation of the hydrogen corona with SPICAM on Mars Express. Icarus, 195, 598–613, doi:10.1016/j.icarus.2008.01.009

Chaufray, J.-Y., Mayyasi, M., Chaffin, M., Deighan, J., Bhattacharyya, D., Clarke, J., et al. (2021). Estimate of the D/H ratio in the Martian upper atmosphere from the low spectral resolution mode of MAVEN/IUVS. Journal of Geophysical Research: Planets, 126, e2020JE006814. https://doi.org/10.1029/2020JE006814

Eparvier, F., Chamberlin, P., Woods, T., Thiemann, E., 2015. The solar extreme ultraviolet monitor for MAVEN. Space Sci. Rev. 195 (1–4), 293–301. doi. org/10.1007/s11214-015-0195-2.

Fedorova, A., Montmessin, F., Korablev, O., Lefèvre, F., Trokhimovskiy, A., & Bertaux, J. (2021). Multi-annual monitoring of the water vapor vertical distribution on Mars by SPICAM on Mars Express. Journal of Geophysical Research: Planets, 126(1), doi. org/10.1029/2020JE006616

Gladstone R. (1982), Radiative transfer with partial frequency redistribution in inhomogeneous atmospheres: Application to the Jovian aurora, Journal of Quantitative Spectroscopy and

Radiative Transfer, Volume 27, Issue 5, Pages 545-556, ISSN 0022-4073, doi.org/10.1016/0022-4073(82)90107-8.

Heavens, N., A. Kleinböhl, M. Chaffin, J. Halekas, D. Kass, P. Hayne, D. McCleese, S. Piqueux, J. Shirley, J. Schofield (2018), Hydrogen escape from Mars enhanced by deep convection in dust storms, Nat. AStro., v 2, 126–132, DOI:10.1038/s41550-017-0353-4

Holmes, J.A., S.R. Lewis, M.R. Patel, M.S. Chaffin, E.M. Cangi, J. Deighan, N.M. Schneider, S. Aoki, A.A. Fedorova, D.M. Kass, A.C. Vandaele (2022), Enhanced water loss from the martian atmosphere during a regional-scale dust storm and implications for long-term water loss, Earth and Planetary Science Letters, 571, 117109, doi.org/10.1016/j.epsl.2021.117109.

Jakosky, B. (2021), Atmospheric Loss to Space and the History of Water on Mars, Annu. Rev. Earth Planet. Sci., 49:71–93, doi.org/10.1146/annurev-earth-062420-052845

Kass, D. M., A. Kleinböhl, D. J. McCleese, J. T. Schofield, and M. D. Smith (2016), Interannual similarity in the Martian atmosphere during the dust storm season, Geophys. Res. Lett., 43, 6111 – 6118, doi:10.1002/2016GL068978.

Kass, D.M., Schofield, J.T., Kleinbohl, A., McCleese, D.J., Heavens, N.G., Shirley, J.H., Steele, L.J., 2019. Mars Climate Sounder observation of Mars' 2018 global dust event. Geophys. Res. Lett., 46, doi.org/10.1029/2019GL083931.

Krasnopolsky, V. A. (2019). Photochemistry of water in the Martian thermosphere and its effect on hydrogen escape. Icarus, 321, 62–70. doi.org/10.1016/j.icarus.2018.10.033

Mayyasi, M., et al., (2017), IUVS echelle-mode observations of interplanetary hydrogen: standard for calibration and reference for cavity variations between earth and Mars during MAVEN cruise, J. Geophys. Res. Space Physics 122. https://doi.org/10.1002/ 2016JA023466.

Mayyasi, M., Bhattacharyya, D., Clarke, J., Catalano, A., Benna, M., Mahaffy, P., et al. (2018). Significant space weather impact on the escape of hydrogen from Mars. Geophysical Research Letters, 45, 8844–8852. https://doi.org/10.1029/ 2018GL07772

Mayyasi, M., Clarke, J., Bertaux, J.-L., Deighan, J., Bhattacharyya, D., Chaffin, M., et al. (2023). Upgrades to the MAVEN Echelle data reduction pipeline: New calibration standard and improved faint emission detection algorithm at Lyman-α. Earth and Space Science, 10, e2022EA002602. https://doi. org/10.1029/2022EA002602

Montmessin, F., Belyaev, D. A., Lefèvre, F., Alday, J., Vals, M., Fedorova, A. A., et al. (2022). Reappraising the production and transfer of hydrogen atoms from the middle to the upper atmosphere of Mars at times of elevated water vapor. Journal of Geophysical Research: Planets, 127, e2022JE007217, doi.org/10.1029/2022JE007217.

Nagy, A. F., J. Kim, and T. E. Cravens, Hot hydrogen and oxygen atoms in the upper atmospheres of Venus and Mars (1990), Ann. Geophys., 8, 251-256.

Pieris, H. and P. Hayne (2023), Possible Thermal Precursor Signal of Martian Dust Storms, AGU Abstract P51F-2768, San Francisco, CA, Dec 2023 (https://agu.confex.com/agu/fm23/meetingapp.cgi/Paper/1418876).

Stone, S. W., Yelle, R. V., Benna, M., Lo, D. Y., Elrod, M. K., & Mahaffy, P. R. (2020). Hydrogen escape from Mars is driven by seasonal and dust storm transport of water. Science, 370(6518), 824–831. doi.org/10.1126/science.aba5229.

Figure 1.

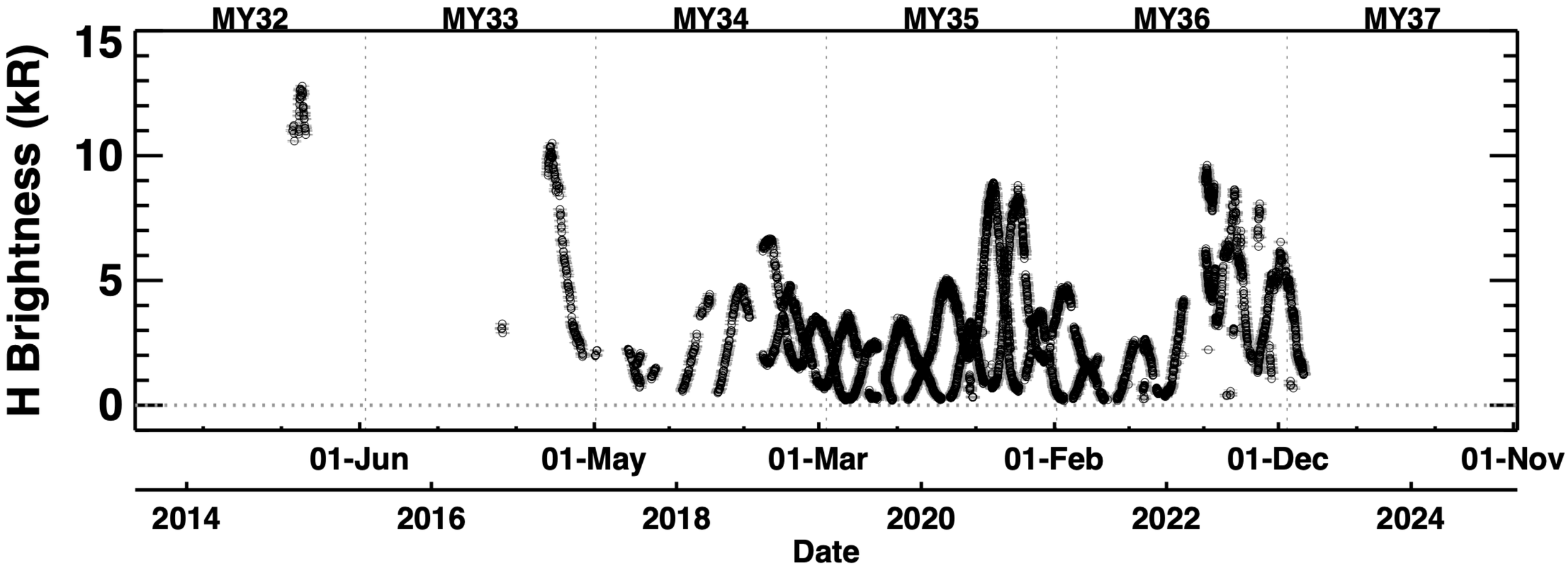
MY32
MY33
MY34
MY35
MY36
MY37
H Brightness (kR)
15
10
5
0
01-Jun
01-May
01-Mar
01-Feb
01-Dec
01-Nov
2014
2016
2018
2020
2022
2024
Date

Figure 2.

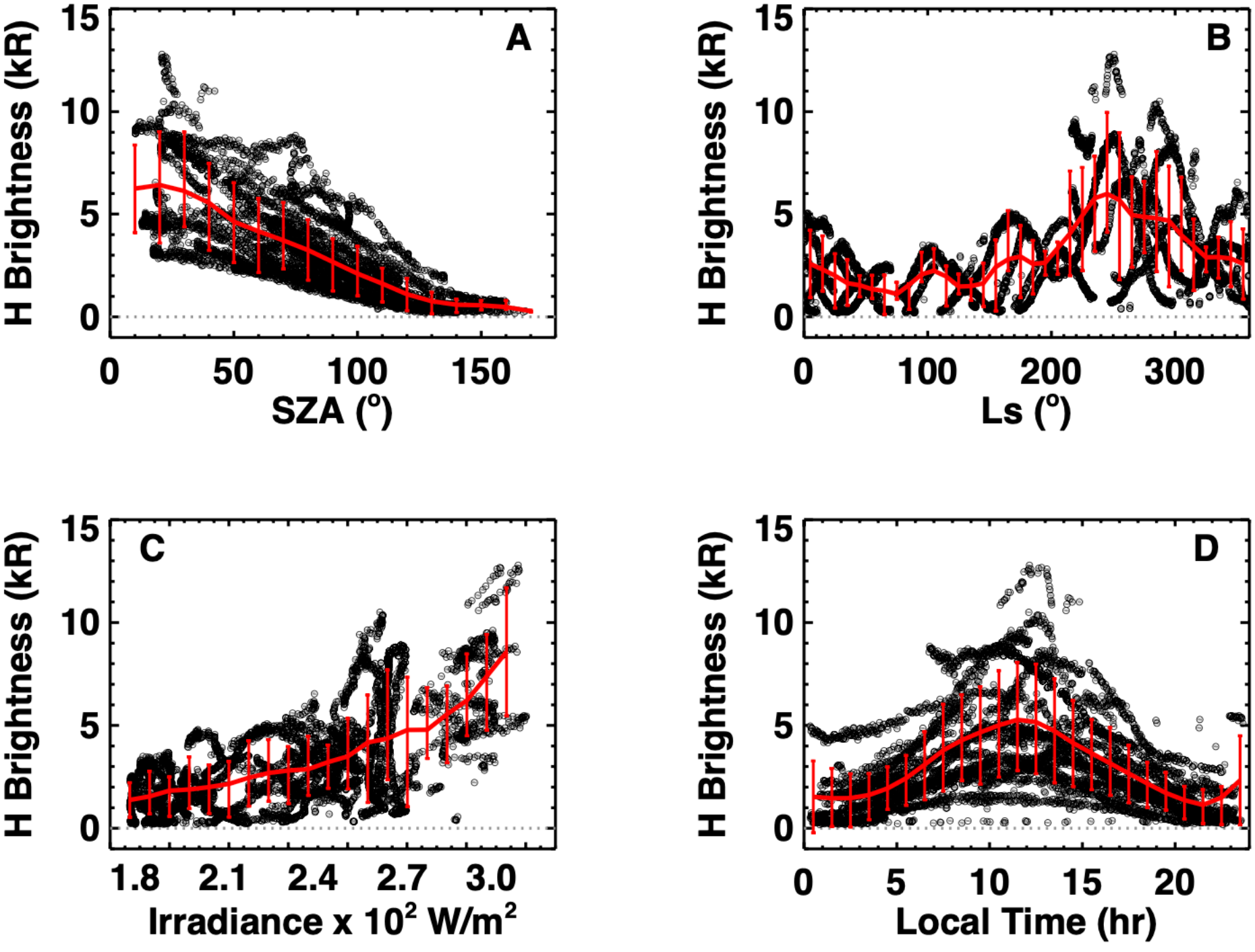
A
H Brightness (kR)
15
10
5
0
0
50
100
150
SZA (°)
B
H Brightness (kR)
15
10
5
0
0
100
200
300
Ls (°)
C
H Brightness (kR)
15
10
5
0
1.8
2.1
2.4
2.7
3.0
Irradiance x 10² W/m²
D
H Brightness (kR)
15
10
5
0
0
5
10
15
20
Local Time (hr)

Figure 3.

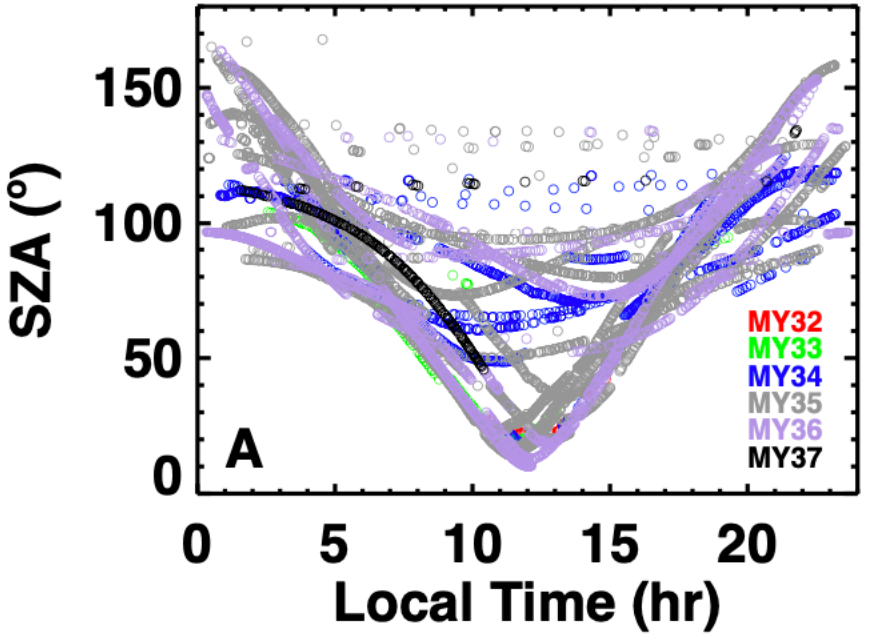
SZA (°)
150
100
50
0
0
5
10
15
20
Local Time (hr)
A
MY32
MY33
MY34
MY35
MY36
MY37

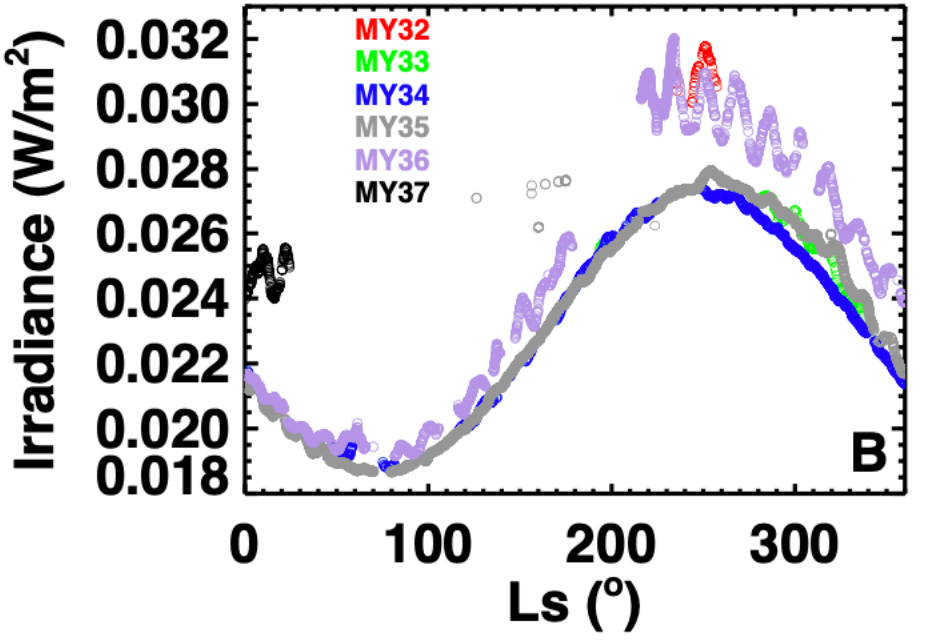
Irradiance (W/m²)
0.032
0.030
0.028
0.026
0.024
0.022
0.020
0.018
0
100
200
300
Ls (°)
B
MY32
MY33
MY34
MY35
MY36
MY37

Figure 4.

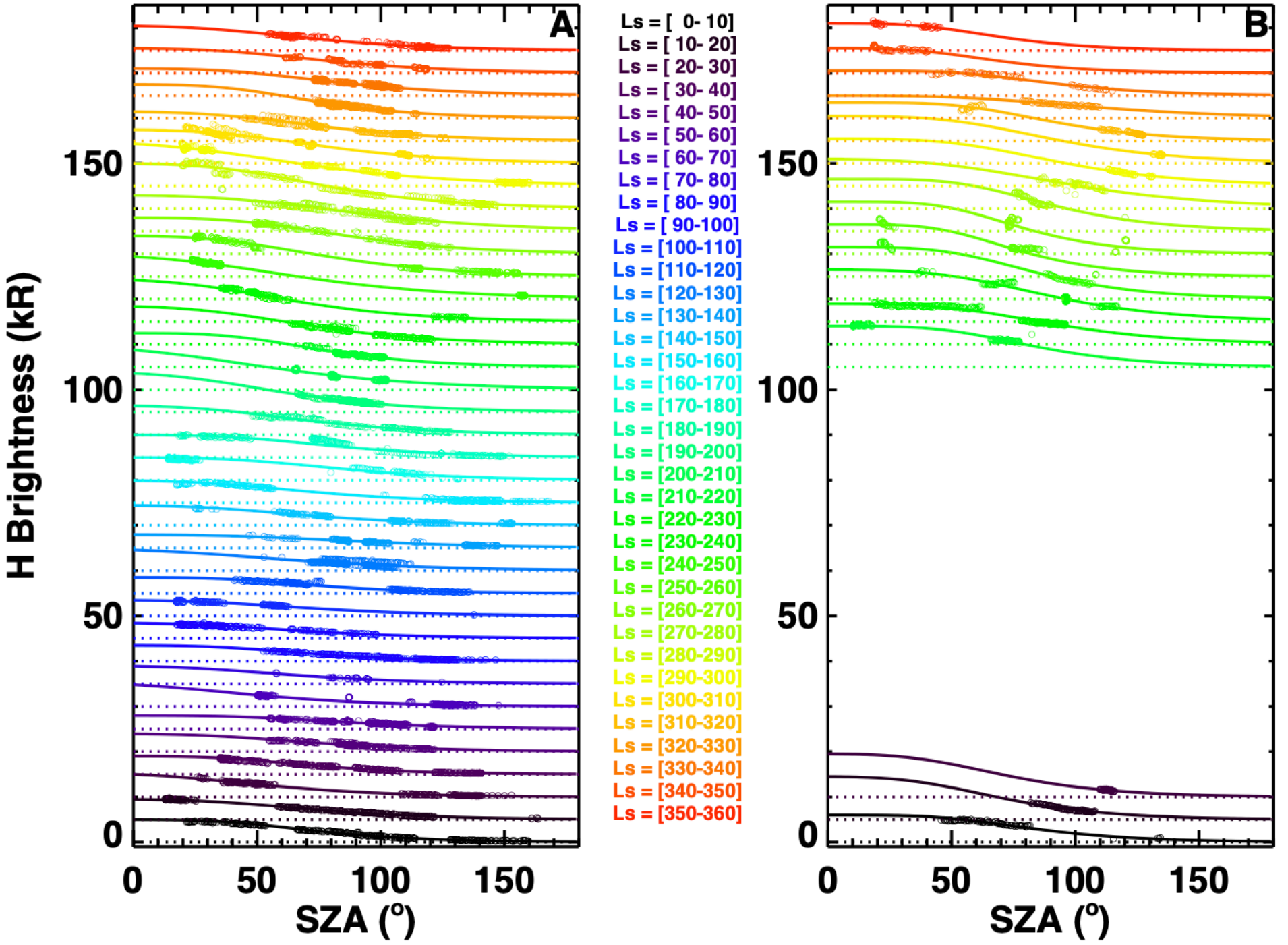
A
B
H Brightness (kR)
0
50
100
150
SZA (°)
Ls = [0- 10]
Ls = [10- 20]
Ls = [20- 30]
Ls = [30- 40]
Ls = [40- 50]
Ls = [50- 60]
Ls = [60- 70]
Ls = [70- 80]
Ls = [80- 90]
Ls = [90-100]
Ls = [100-110]
Ls = [110-120]
Ls = [120-130]
Ls = [130-140]
Ls = [140-150]
Ls = [150-160]
Ls = [160-170]
Ls = [170-180]
Ls = [180-190]
Ls = [190-200]
Ls = [200-210]
Ls = [210-220]
Ls = [220-230]
Ls = [230-240]
Ls = [240-250]
Ls = [250-260]
Ls = [260-270]
Ls = [270-280]
Ls = [280-290]
Ls = [290-300]
Ls = [300-310]
Ls = [310-320]
Ls = [320-330]
Ls = [330-340]
Ls = [340-350]
Ls = [350-360]

Figure 5.

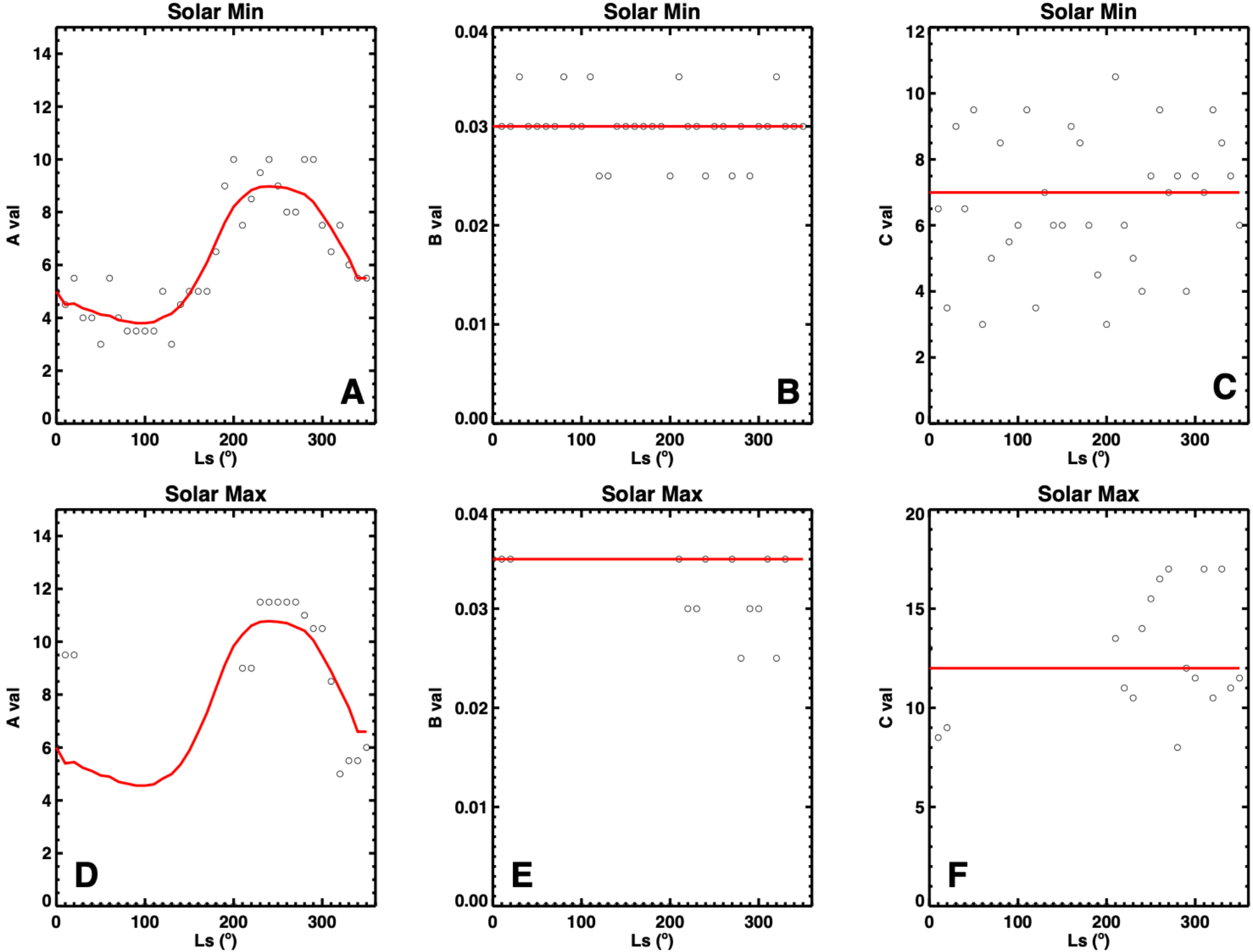
Solar Min
A val
Ls (°)
A
Solar Min
B val
Ls (°)
B
Solar Min
C val
Ls (°)
C
Solar Max
A val
Ls (°)
D
Solar Max
B val
Ls (°)
E
Solar Max
C val
Ls (°)
F

Figure 6.

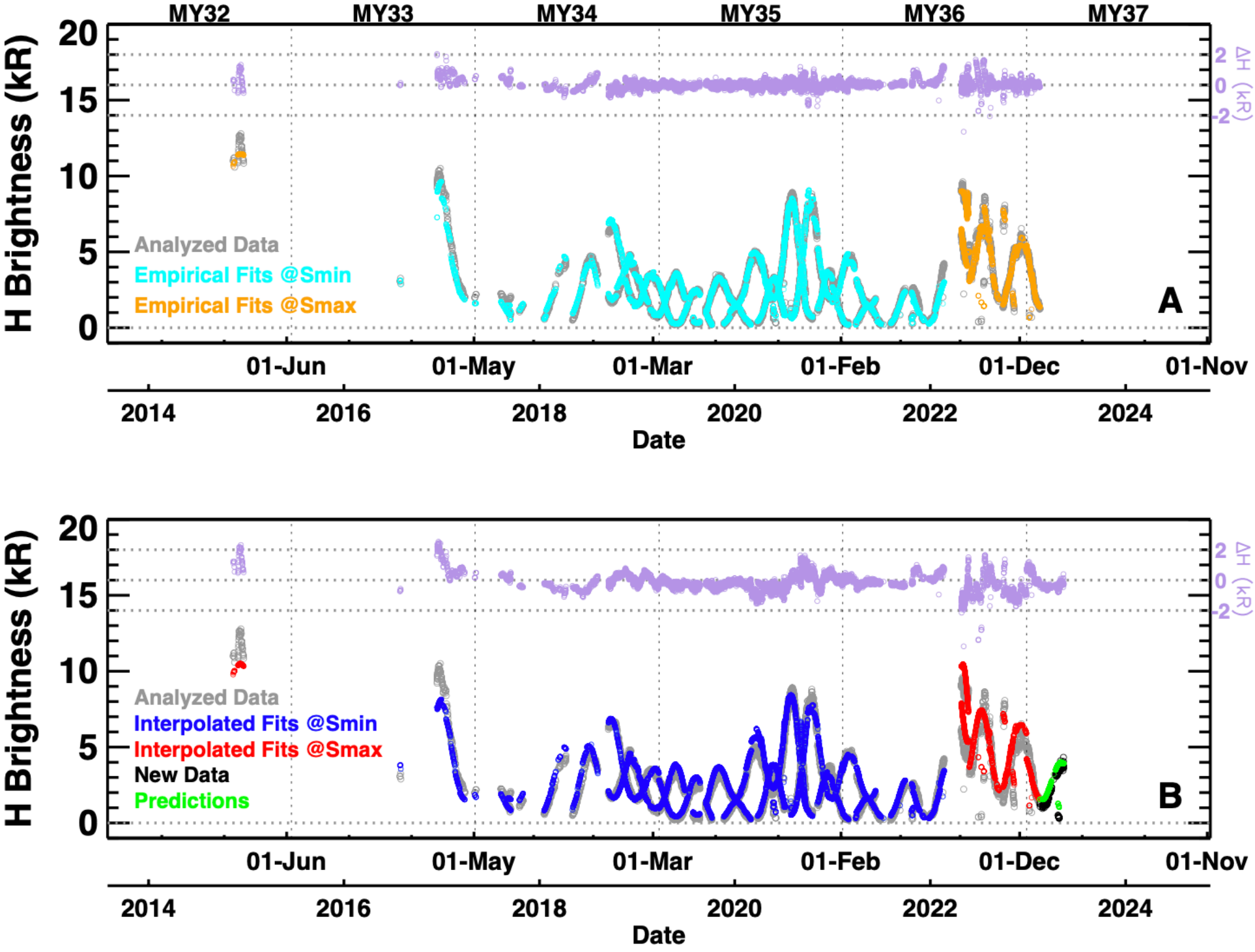
MY32
MY33
MY34
MY35
MY36
MY37
H Brightness (kR)
20
15
10
5
0
ΔH (kR)
2
0
-2
Analyzed Data
Empirical Fits @Smin
Empirical Fits @Smax
A
01-Jun
01-May
01-Mar
01-Feb
01-Dec
01-Nov
2014
2016
2018
2020
2022
2024
Date
H Brightness (kR)
20
15
10
5
0
ΔH (kR)
2
0
-2
Analyzed Data
Interpolated Fits @Smin
Interpolated Fits @Smax
New Data
Predictions
B
01-Jun
01-May
01-Mar
01-Feb
01-Dec
01-Nov
2014
2016
2018
2020
2022
2024
Date

Figure S1.

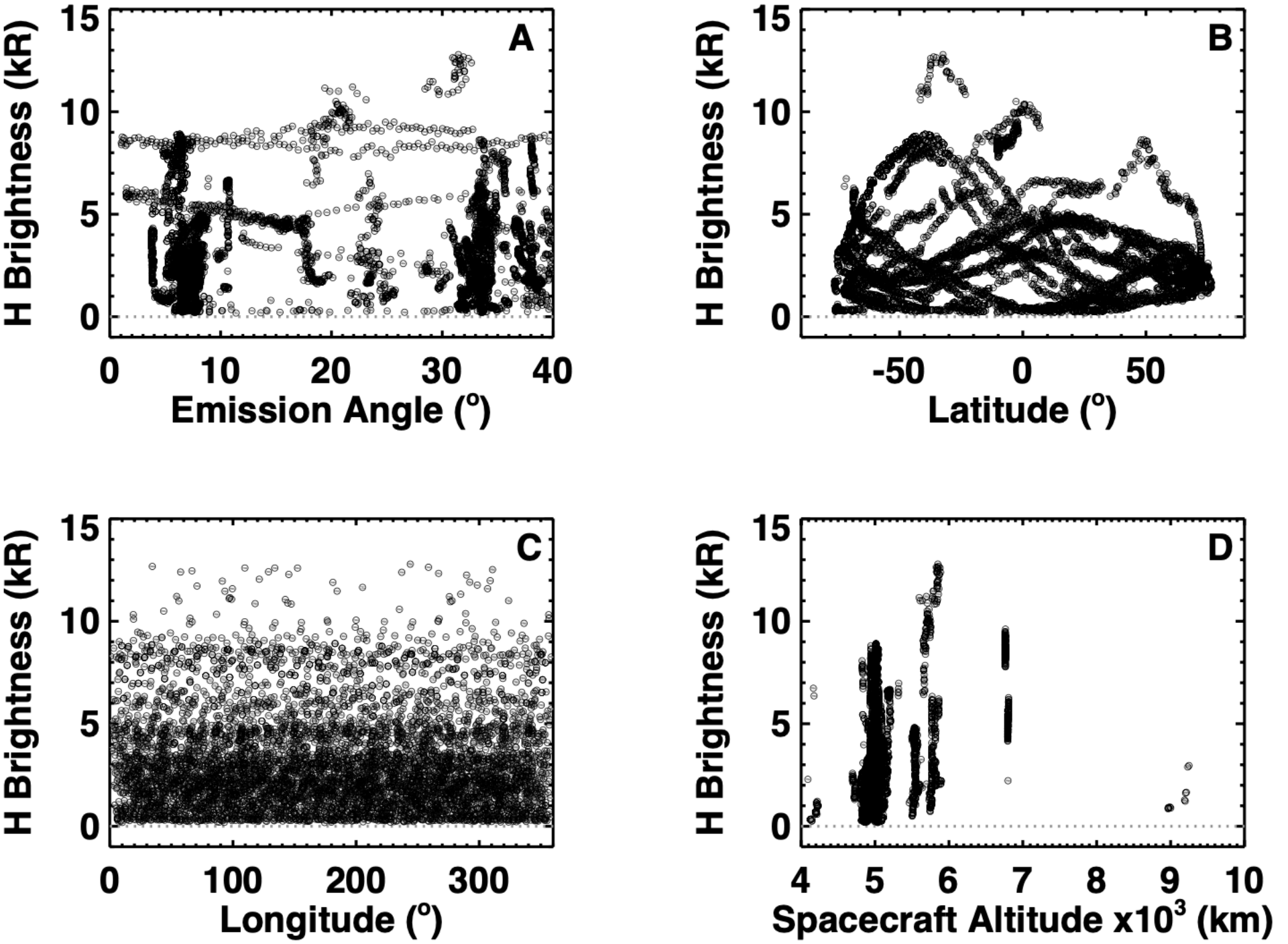
A
H Brightness (kR)
15
10
5
0
0
10
20
30
40
Emission Angle (°)
B
H Brightness (kR)
-50
0
50
Latitude (°)
C
H Brightness (kR)
0
100
200
300
Longitude (°)
D
H Brightness (kR)
4
5
6
7
8
9
10
Spacecraft Altitude x10^3 (km)

Figure S2.

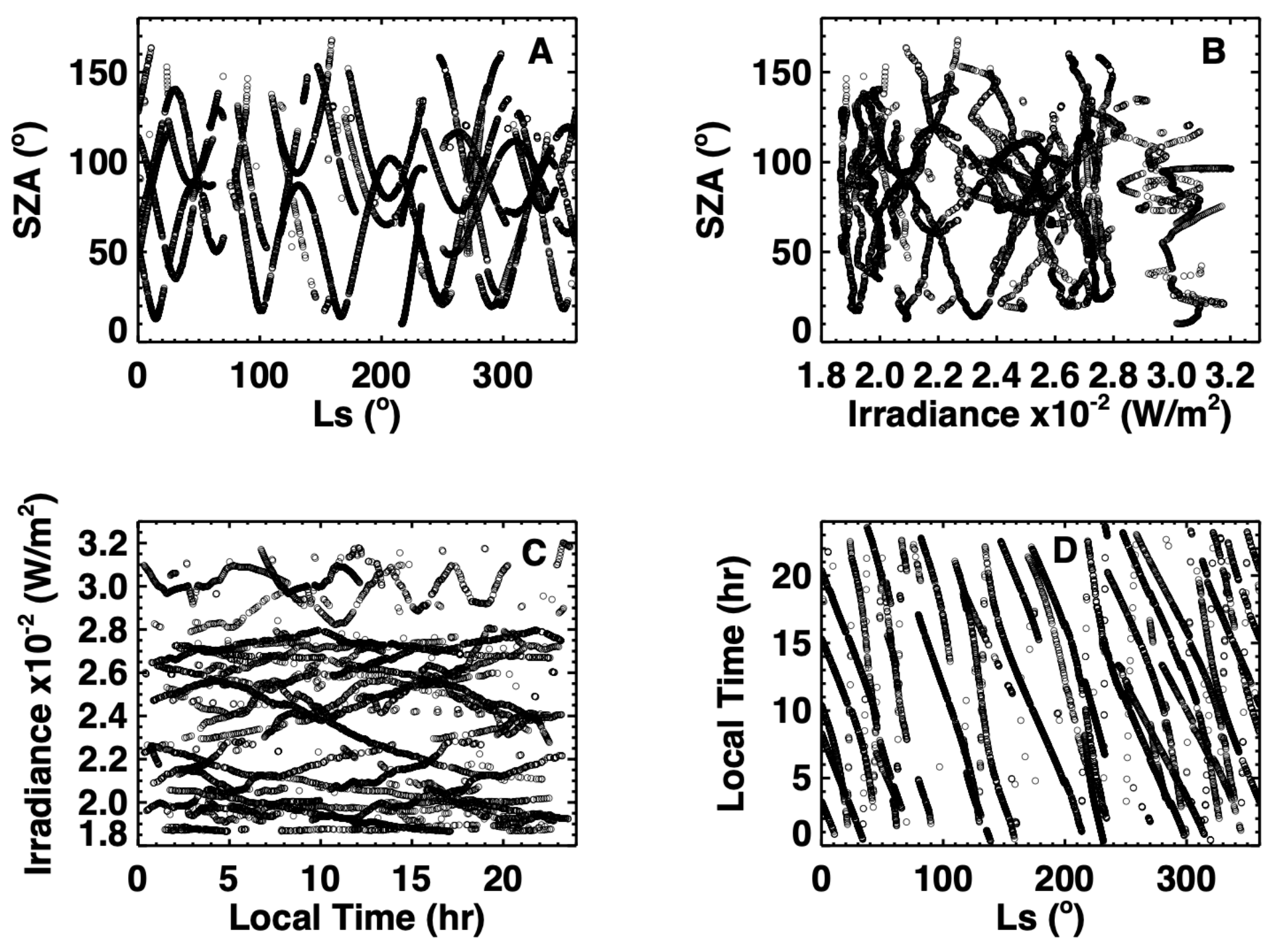
A
SZA (°)
150
100
50
0
0
100
200
300
Ls (°)
B
SZA (°)
150
100
50
0
1.8 2.0 2.2 2.4 2.6 2.8 3.0 3.2
Irradiance x10-2 (W/m2)
C
Irradiance x10-2 (W/m2)
3.2
3.0
2.8
2.6
2.4
2.2
2.0
1.8
0
5
10
15
20
Local Time (hr)
D
Local Time (hr)
20
15
10
5
0
0
100
200
300
Ls (°)

Figure S4.

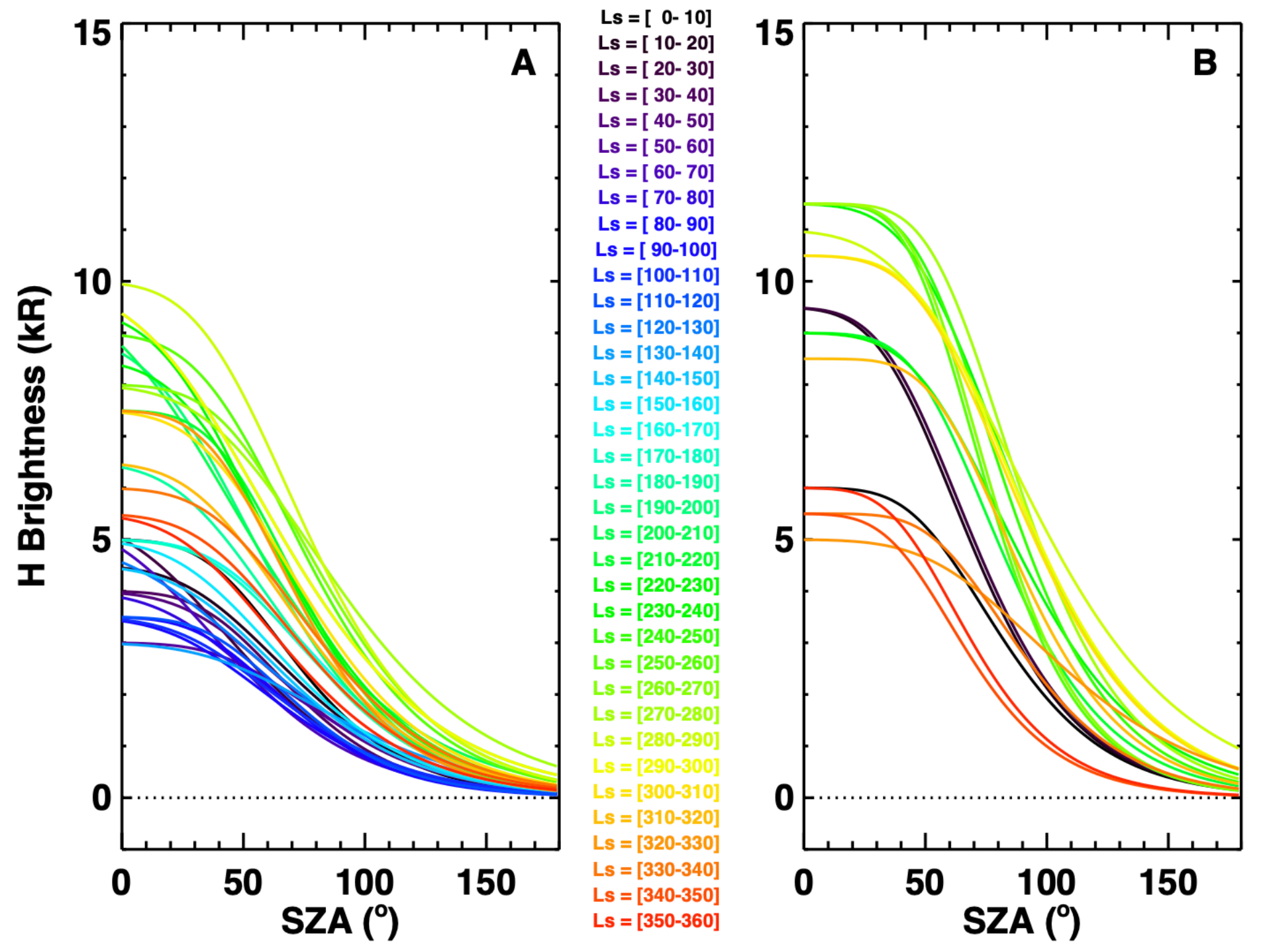
A
B
H Brightness (kR)
SZA (°)
SZA (°)
0
5
10
15
0
50
100
150
Ls = [0- 10]
Ls = [10- 20]
Ls = [20- 30]
Ls = [30- 40]
Ls = [40- 50]
Ls = [50- 60]
Ls = [60- 70]
Ls = [70- 80]
Ls = [80- 90]
Ls = [90-100]
Ls = [100-110]
Ls = [110-120]
Ls = [120-130]
Ls = [130-140]
Ls = [140-150]
Ls = [150-160]
Ls = [160-170]
Ls = [170-180]
Ls = [180-190]
Ls = [190-200]
Ls = [200-210]
Ls = [210-220]
Ls = [220-230]
Ls = [230-240]
Ls = [240-250]
Ls = [250-260]
Ls = [260-270]
Ls = [270-280]
Ls = [280-290]
Ls = [290-300]
Ls = [300-310]
Ls = [310-320]
Ls = [320-330]
Ls = [330-340]
Ls = [340-350]
Ls = [350-360]

Figure S5.

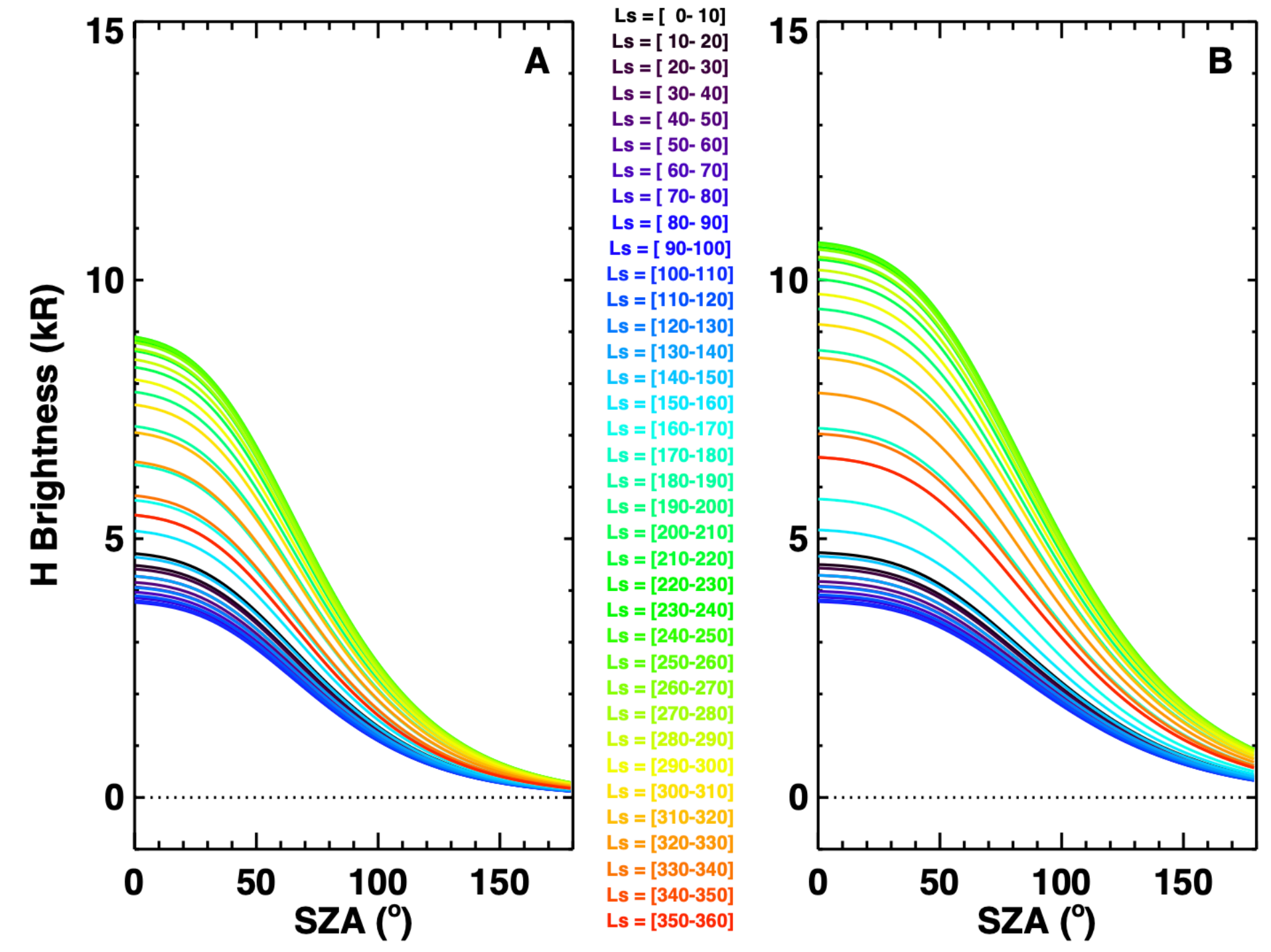
A
B
H Brightness (kR)
SZA (°)
SZA (°)
0
5
10
15
0
50
100
150
Ls = [0- 10]
Ls = [10- 20]
Ls = [20- 30]
Ls = [30- 40]
Ls = [40- 50]
Ls = [50- 60]
Ls = [60- 70]
Ls = [70- 80]
Ls = [80- 90]
Ls = [90-100]
Ls = [100-110]
Ls = [110-120]
Ls = [120-130]
Ls = [130-140]
Ls = [140-150]
Ls = [150-160]
Ls = [160-170]
Ls = [170-180]
Ls = [180-190]
Ls = [190-200]
Ls = [200-210]
Ls = [210-220]
Ls = [220-230]
Ls = [230-240]
Ls = [240-250]
Ls = [250-260]
Ls = [260-270]
Ls = [270-280]
Ls = [280-290]
Ls = [290-300]
Ls = [300-310]
Ls = [310-320]
Ls = [320-330]
Ls = [330-340]
Ls = [340-350]
Ls = [350-360]

Figure S6.

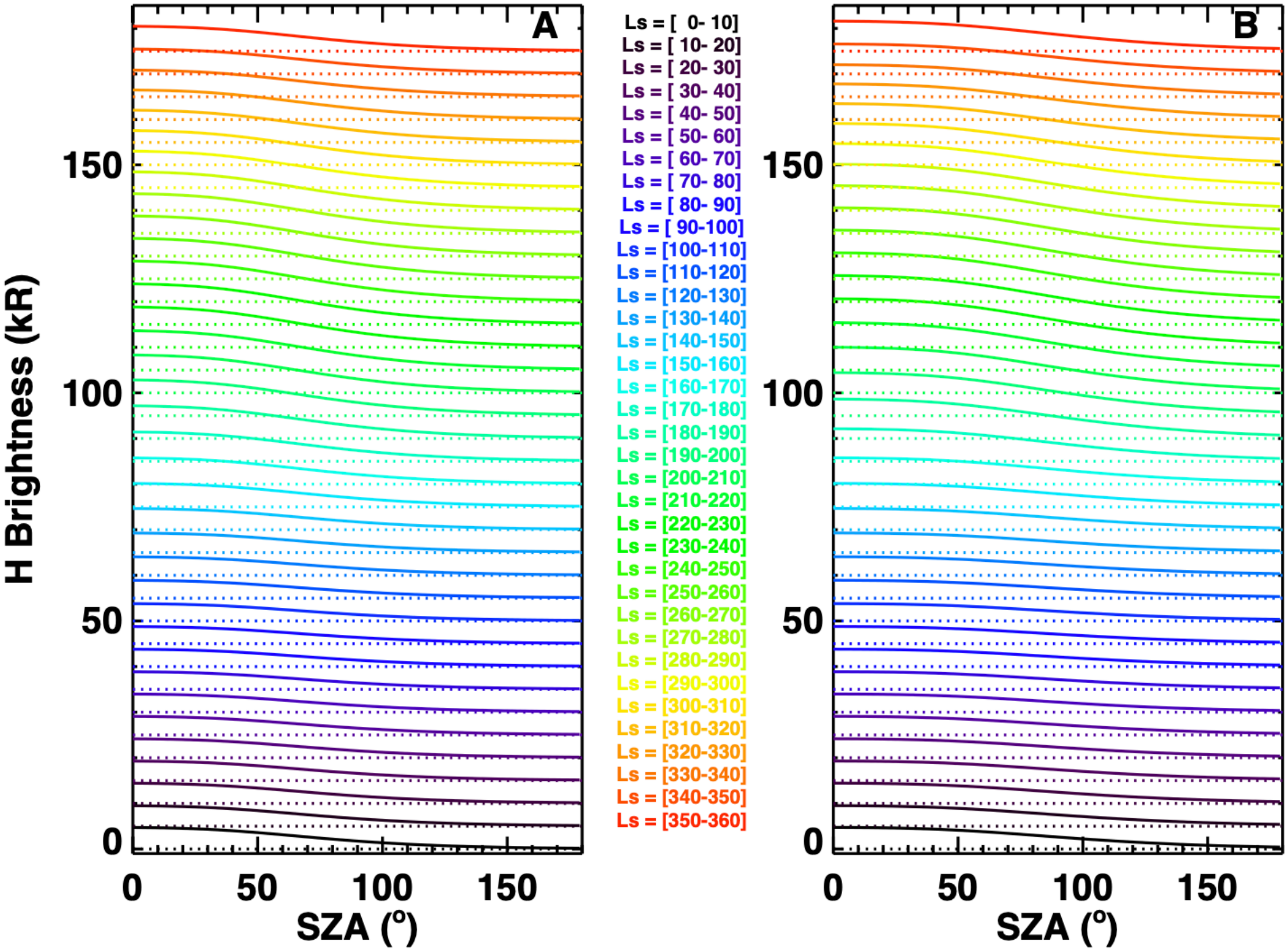
A
B
H Brightness (kR)
0
50
100
150
SZA (°)
Ls = [0- 10]
Ls = [10- 20]
Ls = [20- 30]
Ls = [30- 40]
Ls = [40- 50]
Ls = [50- 60]
Ls = [60- 70]
Ls = [70- 80]
Ls = [80- 90]
Ls = [90-100]
Ls = [100-110]
Ls = [110-120]
Ls = [120-130]
Ls = [130-140]
Ls = [140-150]
Ls = [150-160]
Ls = [160-170]
Ls = [170-180]
Ls = [180-190]
Ls = [190-200]
Ls = [200-210]
Ls = [210-220]
Ls = [220-230]
Ls = [230-240]
Ls = [240-250]
Ls = [250-260]
Ls = [260-270]
Ls = [270-280]
Ls = [280-290]
Ls = [290-300]
Ls = [300-310]
Ls = [310-320]
Ls = [320-330]
Ls = [330-340]
Ls = [340-350]
Ls = [350-360]